



On the development of ice-templated silicon carbide scaffolds for nature-inspired structural materials

Valentina Naglieri^a, Hrishikesh A. Bale^b, Bernd Gludovatz^a, Antoni P. Tomsia^a, Robert O. Ritchie^{a,b,*}

^a Materials Sciences Division, Lawrence Berkeley National Laboratory, Berkeley, CA 94720, USA

^b Department of Materials Sciences & Engineering, University of California, Berkeley, CA 94720, USA

Received 8 June 2013; accepted 2 August 2013

Available online 28 August 2013

Abstract

The processing of ceramic scaffolds using the ice-templating, or freeze casting, technique provides a relatively simple means to mimic the hierarchical design of natural materials such as nacre. In the present study, we investigated the architecture of silicon carbide (SiC) scaffolds produced by this technique over a range of cooling rates and suspension characteristics to demonstrate its versatility and effectiveness for fabricating unidirectional porous bodies with controlled lamella thickness, porosity fraction and morphology. An array of microstructures was generated specifically to examine the role of the suspension solid load and cooling rate on the pore morphology and final ceramic fraction. With respect to the morphology of the pores, a transition from lamellar to dendritic structure was found to be triggered by an increase in cooling rate or in suspension concentration. Similarly, the freezing condition and suspension characteristics were seen to influence the transition between particle rejection and entrapment by the ice. Based on this study, the specific processing parameters that result in distinct scaffold morphologies, namely lamellar, dendritic or isotropic morphology (the latter corresponding to particle entrapment), are identified and presented in the form of a “morphology map” to establish the regions of the different architectures of freeze-cast SiC scaffolds.

Published by Elsevier Ltd. on behalf of Acta Materialia Inc.

Keywords: Ceramics; Silicon carbide; Bioinspired materials; Freeze casting; Scaffolds

1. Introduction

Freeze casting was first developed to fabricate net-shaped dense materials [1–3]; recently, however, this technique has received most interest as a means to produce porous scaffolds by using ice as a template for complex and hierarchical architectures [4–9]. The phenomena exploited in the fabrication of ice-templated porous materials are the same ones occurring during freezing of salt solutions, namely the phase separation and the ejection of the impurities from the ice [10–15].

Freeze casting can offer several advantages compared to other templating techniques; it is a simple method, adaptable for processing different materials [16], enabling a fine control of porosity and wall thickness and manipulation of the surface roughness [17,18]. When applied to ceramic processing, this technique comprises the unidirectional freezing of a slurry. While the liquid, either water or an organic solvent, solidifies under the constraint imposed by a thermal gradient, the ceramic particles are ejected and entrapped in the space between the ice crystals, leading to the formation of alternating lamellae of ice and ceramic. After sublimation of the ice and sintering, a ceramic scaffold exhibiting unidirectional pores is obtained that is the negative replica of the ice crystals. The details of the process have been widely discussed in literature, with several investigations describing the

* Corresponding author at: Department of Materials Sciences & Engineering, University of California, Berkeley, CA 94720, USA. Tel.: +1 510 486 5798; fax: +1 510 643 7294.

E-mail address: roritchie@lbl.gov (R.O. Ritchie).

influence of such factors as the solvents, particle size, suspension solid content, additives, cooling rate and freezing temperature on the final microstructure of the scaffold [19–24].

Unidirectional porous materials are needed for a broad range of applications, such as filters, membranes, catalyst supports and load-bearing structures. Moreover, unidirectional porous and composite structures are common in nature, since their design enables the optimization of the mechanical properties [25] according to their specific function. To this end, the architectures of natural materials such as nacre, bone, wood, etc., have been considered as models for the development of new synthetic materials [26]. Deville et al. [8] first pointed out the similarities between the freeze-cast scaffolds and the inorganic component of nacre, thereby demonstrating the utility of this processing technique for the biomimicry of natural structures with multiple characteristic length-scales. Specifically, these authors mimicked the hierarchical structure of nacre by producing a scaffold made of parallel inorganic layers, whose surface roughness and characteristic bridges between lamellae resembled the features of the aragonite platelets [8]. The result was alumina composites obtained by infiltrating the ceramic scaffold with either a polymer (epoxy) or a metal (Al–Si alloy); in this manner synthetic nacre-like materials were processed with a lamellar structure and ceramic content up to ~45 vol.% [8]. In subsequent studies [27], the processing was modified to yield alumina/PMMA materials with up to 80 vol.% ceramic in a more realistic nacre-like “brick-and-mortar” structure. Using strong interfaces between the ceramic and polymeric phases achieved through grafting techniques, these new materials displayed unprecedented levels of toughness for ceramics [27].

As the alumina hybrid materials described above had a relatively low strength (~200 MPa) [27], we describe here our initial studies to make higher-strength “nacre-like” materials using freeze casting to produce scaffolds of silicon carbide, the choice of SiC being motivated by its high hardness and low specific weight. Although many ceramics have now been processed by this method, few studies have focused on SiC [28,29], possibly because it is more difficult to sinter and requires higher temperatures and controlled atmospheres. Our aim here is to investigate the architecture of freeze-cast SiC scaffolds over a range of cooling rates and suspension characteristics, to generate a morphology map to identify the most suitable conditions for the development of unidirectionally porous silicon carbide structures. Although explanations of the freeze casting process are well described in the literature [17,18,20–24], it is quite difficult to find comprehensive reviews able to account for the various conditions used and the resulting morphologies observed. What follows is an attempt to provide an overall explanation for most of the phenomena while remaining consistent with the experimental data.

2. Experimental procedures

Silicon carbide is one of the most promising materials for high temperature structural components, due to its excellent strength, hardness and oxidation resistance. These properties, as well as its “sintering resistance”, result from the covalent nature of the Si–C bond and its low self-diffusion coefficient [30]. Liquid-phase sintering has to be carried out to induce effective densification in SiC bodies at temperatures of 1750–2000 °C, lower than those usually involved in solid-state sintering (~2100 °C) [31].

Two commercial silicon carbide powders, purchased from ABCR GmbH & Co. KG, Karlsruhe, Germany, were used: α -SiC (UF-15) and β -SiC (BF-17), respectively, with mean particle sizes of 0.55 and 0.50 μm and specific surface areas of 15 and 17 $\text{m}^2 \text{g}^{-1}$, as reported by the supplier. Alumina (Ceralox SPA05, Ceralox Div., Condea Vista Co., Tucson, AZ) and yttria (Grade C, ABCR GmbH & Co. KG, Karlsruhe, Germany) were added as aids for the liquid-phase sintering [32–36], with a $\text{Al}_2\text{O}_3/\text{Y}_2\text{O}_3$ molar ratio of 5/3 kept constant for all suspensions, corresponding to the stoichiometric ratio of the YAG ($\text{Y}_3\text{Al}_5\text{O}_{12}$) phase.

The suspensions were obtained by mixing SiC powders and the sintering aids (10 wt.% total amount with respect to SiC) in deionized water. A β -SiC/ α -SiC weight ratio of 95/5 was chosen to promote $\beta \rightarrow \alpha$ phase transformation, yielding a microstructure with elongated grains [37,38], which is known to promote toughening in SiC by crack bridging and deflection [39].

Slurries were prepared with solid contents of 17, 23, 25 and 30 vol.%; these suspensions are hereafter referred to as SiC17, SiC23, SiC25 and SiC30, respectively. The dispersion was performed by adding ammonium hydroxide (NH_4OH) to the slurries in order to adjust the pH at 10 [40], and by ball milling for 40 h. Polyethylene glycol (PEG) was used as an organic binder, and added to the suspensions before freeze casting.

To conduct the freeze casting, the slurry was poured into a Teflon mold (diameter: 35 mm, height: 30 mm), which was placed on the top of a cold finger and stabilized at 3 °C. The cold finger was then cooled by liquid nitrogen at a controlled rate between -1 and -15 °C min^{-1} (with a precision of $\sim\pm 3$ °C). The average freezing front velocity, v , for each sample was defined as the time to complete the solidification divided by the actual height of the sample.

For each suspension, a series of samples was produced at different cooling rates. For example, for the SiC17 suspension, samples were freeze-cast at -1 , -5 , -10 and -15 °C min^{-1} ; these were termed, respectively, SiC17-1, SiC17-5, SiC17-10 and SiC17-15. The suspension compositions and cooling rates applied to each sample are listed in Table 1. Procedures and the specific equipment for the freeze casting are described in detail elsewhere [17].

After freeze drying (Freeze Dryer 8, Labconco, Kansas City, MI) for 24–48 h, the green bodies were treated at

Table 1
Details of suspension compositions and cooling rates studied.

Suspension	Solid content	Additives	Sample	Cooling rate (°C min ⁻¹)
SiC17	17 vol.%	NH ₄ OH, 5 wt.% PEG	SiC17-1	-1
			SiC17-5	-5
			SiC17-10	-10
			SiC17-15	-15
SiC23	23 vol.%	NH ₄ OH, 5 wt.% PEG	SiC23-10	-10
			SiC23-15	-15
SiC25	25 vol.%	NH ₄ OH, 5 wt.% PEG	SiC25-1	-1
			SiC25-5	-5
			SiC25-10	-10
SiC30	30 vol.%	NH ₄ OH, 5 wt.% PEG	SiC30-1	-1
			SiC30-5	-5
			SiC30-10	-10

450 °C for 4 h to burn out the organic additives, and then sintered at 1800–1900 °C for 30 min to 4 h, in a graphite furnace (Model 1000-4560-FP30, Thermal Technologies Inc., Santa Rosa, CA), under an argon atmosphere.

Microstructures were investigated using scanning electron microscopy (SEM, S-4300SE/N, Hitachi, Pleasanton, CA). Fig. 1 shows an example of a micrograph of a freeze-cast scaffold consisting of parallel ceramic lamellae which are connected by characteristic bridges (marked by red arrows). To characterize the nature of the lamellar microstructures, the lamella thickness, δ , the spacing (wavelength) of the lamellae, λ , (Fig. 1) and the ceramic volume fraction were evaluated using image analysis on scanning electron micrographs; a sufficient number of measurements (>100) was performed to obtain a reasonably small confidence interval for the mean values of δ and λ . The morphology of the scaffolds was characterized in terms of the number of ceramic bridges between adjacent lamellae per unit area (bridge density, ρ_b). As the bridge density is invariably related to the lamella wavelength, λ , a dimensionless parameter m was defined as:

$$m = (1/\rho_b)/\lambda^2 \quad (1)$$

This parameter comprises the inverse of the bridge density, $1/\rho_b$ (which is the square of the spacing of the bridges), divided by the square of the wavelength of the lamellae. It fully describes the morphology of the scaffold and distinguishes between the various forms, namely lamellar, dendritic or isotropic structures. We identified as lamellar the structures with low ρ_b and $m > 5$. For $1 < m < 5$, the bridge spacing and the wavelength λ were comparable and the structures were considered as dendritic. For structures characterized by $m < 1$, the spacing between the numerous bridges was smaller than the wavelength. Those scaffolds exhibited a mostly isotropic structure rather than unidirectional. Details of these three scaffold morphologies are described in the following sections.

Three-dimensional (3-D) architectures of the SiC25-1 and SiC25-5 scaffolds were characterized using X-ray

computed micro-tomography (X-ray μ CT) at beamline 8.3.2 of the Advanced Light Source, Berkeley CA. The samples were ground to a cross-sectional size of 1 mm \times 1 mm to fit into the camera's field of view. The samples were scanned at a resolution of 1.3 μ m per pixel at X-ray energy of 27 keV and 3-D tomography data were generated by reconstructing slices from 900 X-ray projections collected over a 180° sample rotation. The 3-D datasets were visualized in Avizo 6.1 (Visualization Sciences Group, Burlington, MA, USA) and quantitatively analyzed for the 3-D lamella thickness and spacing in ImageJ (Rasband, W.S., ImageJ, US National Institutes of Health, Bethesda, Maryland, USA).

3. Results

3.1. Relationship between cooling rate and freezing front velocity

The velocity of the freezing solid–liquid interface depends on the imposed temperature gradient, which can be modified by tuning the cooling rate, and the thermal properties of the solidifying layer. In the present work, linear cooling rates were used in the range of -1 to -15 °C min⁻¹ to obtain more uniform lamellar structures. The relationship between the cooling rate, measured at the top of the cold finger, and the freezing front velocity, obtained by dividing the time to freeze by the height of the sample, is shown in Fig. 2. For all the slurries studied, the freezing front velocity was found to be linearly related to the cooling rate, with the slope of the relationship depending on the specific composition and SiC concentration.

3.2. Influence of the freezing front velocity on the lamella thickness and wavelength

For all the series of scaffolds examined, the lamella thickness and wavelength, which were evaluated by image

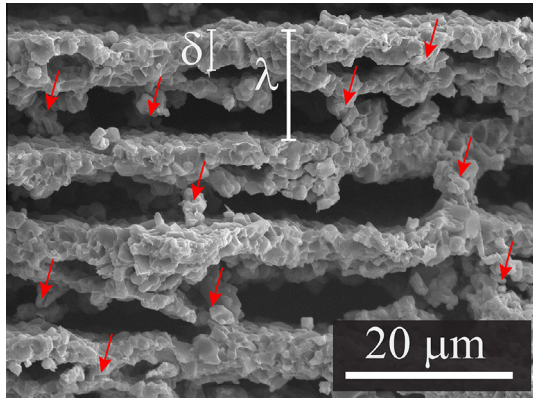


Fig. 1. SEM micrograph of a SiC scaffold obtained by freezing a suspension with 17 vol.% solid load at $-10\text{ }^{\circ}\text{C min}^{-1}$, sintered at $1900\text{ }^{\circ}\text{C}$ for 1 h, showing the parallel lamellae connected by the characteristic bridges (arrows). The lamella thickness and the wavelength, respectively, are defined by δ and λ , as depicted.

analysis on SEM micrographs, were found to decrease with increasing freezing front velocity. The dependence of the lamella thickness and wavelength on the average freezing front velocity for SiC17 scaffolds, obtained from the suspensions with 17 vol.% solid load, are shown in Fig. 3a and b. Results show that the lamella thickness δ can be reduced by half, from ~ 6 to $3\text{ }\mu\text{m}$, when the freezing front velocity is increased from 15 to $45\text{ }\mu\text{m s}^{-1}$ (cooling rate increased from -1° to $-15\text{ }^{\circ}\text{C min}^{-1}$). A similar trend was observed for the wavelength; the relationship between λ and the average freezing front velocity v can be approximated by the following power law: $\lambda = Av^{-n}$. For the SiC17 samples, the exponent n was ~ 0.85 , which is close to the values reported in literature for suspensions of ceramic particles with similar size [20,41].

SEM images, shown in Fig. 4 for SiC17 samples, reveal that increasing cooling rates (and hence freezing front velocities) cause structural refinement in the form of thinner scaffold walls, consistent with the data in Fig. 2. As the freezing front velocities increase, the pore morphology changes from that of lamellar pores at $\sim 5\text{--}25\text{ }\mu\text{m s}^{-1}$ (Fig. 4a and b) to dendritic pores, with smaller aspect ratios and a higher density of bridges between the ceramic walls at $\sim 30\text{--}45\text{ }\mu\text{m s}^{-1}$ (Fig. 4c and d).

SiC25-1 and SiC25-5 scaffolds, obtained from suspensions with solid loads of 25 vol.%, frozen respectively at -1° and $-5\text{ }^{\circ}\text{C min}^{-1}$, were characterized by X-ray μCT . The 3-D tomography images and the respective two-dimensional (2-D) slices (cross-sections perpendicular to the direction of freezing) for these two samples are shown in Fig. 5a and b. The SiC25-1 sample, frozen at a lower cooling rate than the SiC25-5 scaffold, exhibits a coarser and lamellar structure, whereas the SiC25-5 scaffold has a finer dendritic morphology. In both the samples, the ceramic lamellae are continuous along the scaffolds, parallel to the direction of ice growth.

Quantitative analyses on the 3-D tomography images were performed for the evaluation of the lamella thickness and pore size; results are visualized in Fig. 6. The data for

the lamella thickness (Fig. 6a and c) are consistent with the values obtained by image analysis on SEM micrographs of the same samples. Indeed, mean lamella thicknesses of 19 and $9\text{ }\mu\text{m}$ were measured on the SEM micrographs of the SiC25-1 and SiC25-5 scaffolds, respectively. Furthermore, the analyses of the 3-D tomography images are of particular interest as they reveal the homogeneity of the freeze-cast microstructures across all the samples. The lamella thickness and the pore size are constant along the direction of solidification, demonstrating that the cooling conditions were even during the freezing process.

3.3. Influence of solid load on the lamella thickness and wavelength

Fig. 7a and b shows the measurements of lamella thickness δ and spacing λ for scaffolds prepared from suspensions with solid loads in the range of 17–30 vol.%, all frozen at the same cooling rate of $-1\text{ }^{\circ}\text{C min}^{-1}$. Both δ and λ are seen to be linearly proportional to the solid content, with the lamella thickness varying between 6 and $23\text{ }\mu\text{m}$ and the wavelength between 25 and $50\text{ }\mu\text{m}$.

SEM images of the samples freeze-cast from suspensions with different SiC concentrations and obtained over a range of cooling conditions indicate that only samples frozen at $-1\text{ }^{\circ}\text{C min}^{-1}$ exhibit pure lamellar structures regardless of the solid content in the slurry. For higher cooling rates, the pore morphology depends on the starting solid content, as depicted by SEM micrographs of samples frozen at $-5\text{ }^{\circ}\text{C min}^{-1}$ (Fig. 8). For that particular cooling rate, only the SiC17-5 scaffold displayed a lamellar structure, whereas SiC25-5 and SiC30-5 scaffolds show a more dendritic pattern, with increasing disorder.

The SiC25-10 and SiC30-10 scaffolds did not display a unidirectional microstructure, as the combination of cooling rate and solid content promoted the entrapment of particles in the ice rather than their ejection.

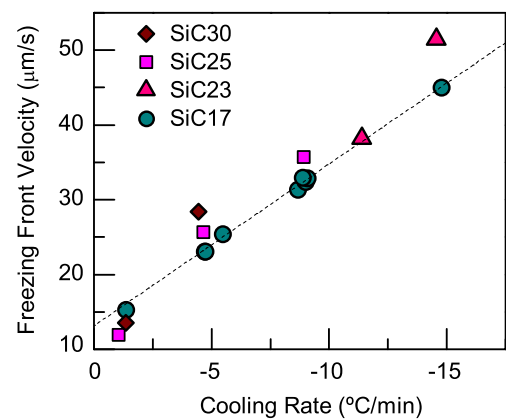


Fig. 2. Relationship between the cooling rate and the average freezing front velocity for various freeze-cast suspensions of SiC. The key to labels for the suspensions is given in Table 1.

3.4. Influence of solid load and freezing front velocity on ceramic content

Data on the ceramic content of the freeze-cast scaffolds, assessed using image analysis of the SEM micrographs, are shown in Fig. 9. The final ceramic content of the scaffolds depends on both the concentration of the starting suspensions and the freezing conditions. As expected for similar cooling rates, more concentrated suspensions lead to higher ceramic contents, e.g., at $-1^\circ\text{C min}^{-1}$, scaffolds with ceramic fractions of ~ 50 , 57 and 67 vol.% were respectively obtained from suspensions with 17, 25 and 30 vol.% solid load. For samples with the same starting composition, the faster the freezing front velocity resulting from a faster cooling rate, the higher the final ceramic content.

3.5. Quantitative characterization of scaffold morphologies

The qualitative differences between lamellar, dendritic and isotropic morphologies were highlighted in the previous sections. The shape of the pores and frequency of ceramic bridges between the main lamellae were seen to change depending on the cooling rate and the suspension concentration. The morphologies of scaffolds from suspensions with 17–30 vol.% solid load, frozen at cooling rates in the range -1° to $-15^\circ\text{C min}^{-1}$, were characterized in terms of bridge density, ρ_b . The results (Fig. 10) revealed that ρ_b increased exponentially with the freezing front velocity for all the samples. However, the bridge density is not sufficient to compare scaffolds obtained from suspensions with different solid loads or to discern between lamellar, dendritic and isotropic morphologies. Indeed the processing parameters also affect the structural wavelength, as the increase in cooling rate induces a structural refinement and more concentrated slurries yield coarser microstructures. Both the bridge density and lamellar wavelength are accounted for by the dimensionless parameter m , defined in Eq. (1); calculated values are plotted in Fig. 11. The SiC17-1, SiC17-5, SiC25-1 and SiC30-1 scaffolds exhibited $m > 5$. For these samples, which were obtained from suspensions with 17, 25 or 30 vol.% solid loads and frozen at $-1^\circ\text{C min}^{-1}$, or from the slurry with

17 vol.% frozen at $-5^\circ\text{C min}^{-1}$, the bridge spacing was large compared to the lamella wavelength. The microstructure of these samples was considered to be lamellar, since few ceramic bridges connected the main lamellae and the pores were extensively elongated. For the SiC17-10, SiC17-15, SiC23-10, SiC23-15 and SiC25-5 scaffolds, m was between 1 and 5, indicating that the bridge spacing approached the lamella wavelength as the cooling rates were increased or more concentrated suspensions were processed. Under these processing conditions, due to the numerous bridges between the main lamellae, tortuous pores with smaller aspect ratio were observed and the scaffolds exhibited a dendritic structure. For the SiC30-5 scaffold, which was generated from a suspension with 30 vol.% solid load frozen at $-5^\circ\text{C min}^{-1}$, a value of $m < 1$ was calculated. The microstructure of this sample was very intricate, at the limit between dendritic and isotropic. The parameter m was not obtained for SiC25-10 and SiC30-10 samples, as the microstructures of these samples did not exhibit a clear unidirectional arrangement. For suspensions with 25 and 30 vol.% solid load frozen at $-10^\circ\text{C min}^{-1}$, the directional growth of ice lamellae was hindered by particle entrapment in the ice.

4. Discussion

4.1. Relationship between cooling rate and freezing front velocity

The velocity of the freezing front depends on the temperature gradient between the solidifying layer and the copper plate, as well as on the thermal properties of the medium through which the enthalpy of solidification is conducted away [42]. Several studies [41,43,44] have shown the disadvantage of a constant temperature applied to the base of the mold, as compared to a linear or parabolic cooling rate. Indeed, a constant temperature at the copper plate reduces the solidification velocity during the freezing process, causing an increasing lamella spacing along the sample length. Conversely, when a linear cooling rate is applied, the decrease in heat conduction caused by the growing ice layer is partially compensated for, with the

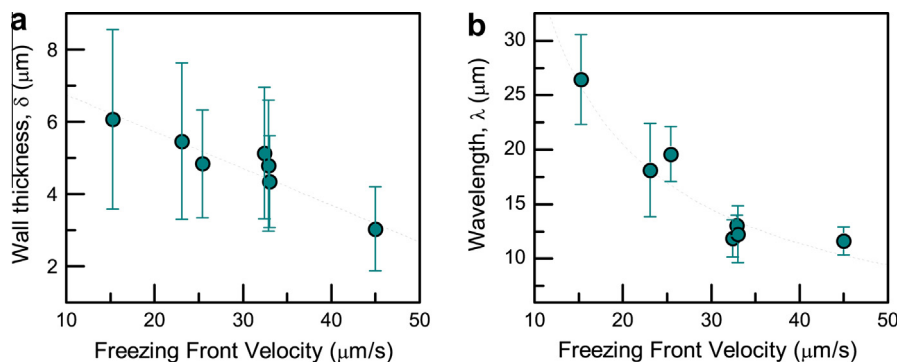


Fig. 3. (a) Lamella wall thickness, δ , and (b) wavelength, λ , as a function of the average freezing front velocity, v , for SiC17 suspensions (17 vol.% solid load), showing that increasing the freezing front velocity induces structural refinement.

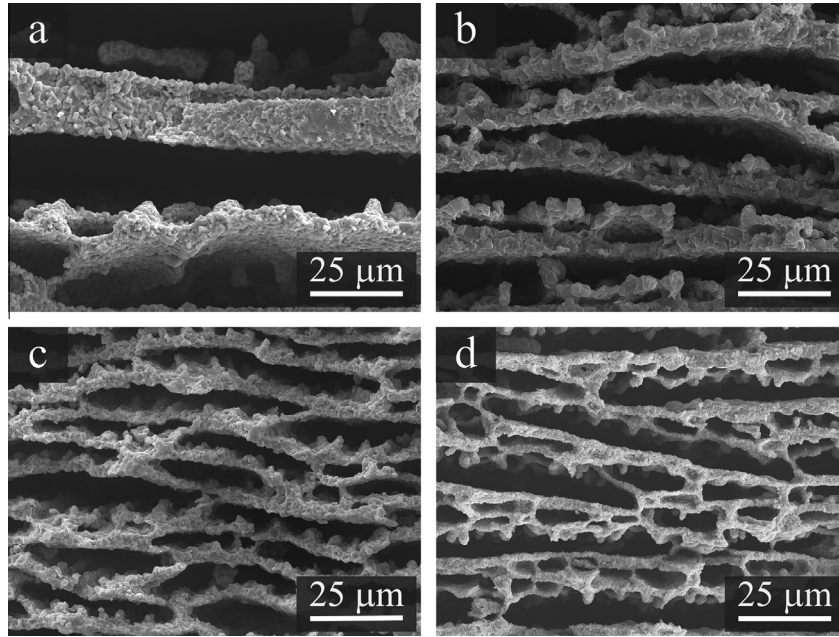


Fig. 4. SEM micrographs of scaffolds from SiC17 suspension (17 vol.% solid load) processed at increasing freezing rates of -1 to -15 $^{\circ}\text{C min}^{-1}$, showing that an increase in cooling rate induces both structural refinement and a morphological transition. Samples (a) SiC17-1 and (b) SiC17-5, frozen at -1 and -5 $^{\circ}\text{C min}^{-1}$, respectively, exhibit lamellar structures. Higher cooling rates, namely (c) -10 $^{\circ}\text{C min}^{-1}$ for the SiC17-10 and (d) -15 $^{\circ}\text{C min}^{-1}$ for the SiC17-15 sample, lead to finer dendritic structures. All samples were sintered at 1850 $^{\circ}\text{C}$ for 1 h.

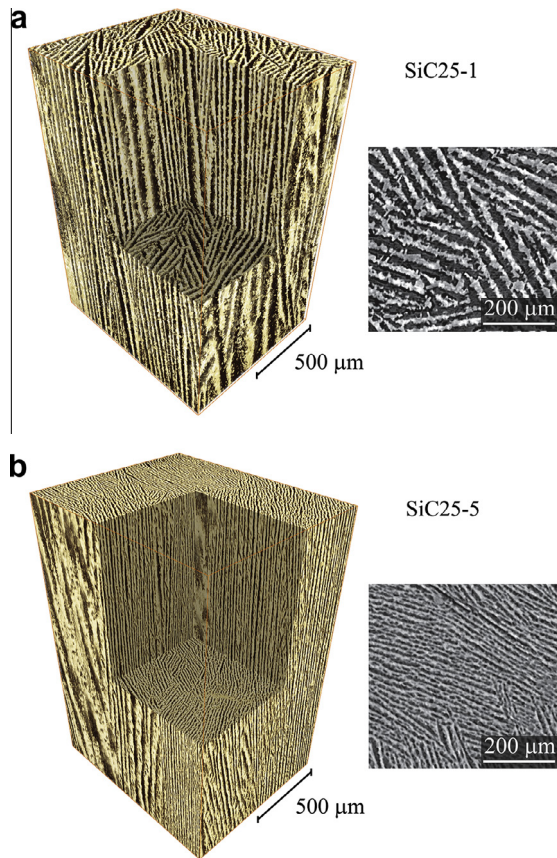


Fig. 5. 3-D X-ray micro-tomography images and 2-D reconstructed slices of (a) SiC25-1 and (b) SiC25-5 scaffolds. The scaffolds were obtained from suspensions at the same concentration (25 vol.%) frozen at (a) -1 and (b) -5 $^{\circ}\text{C min}^{-1}$, respectively.

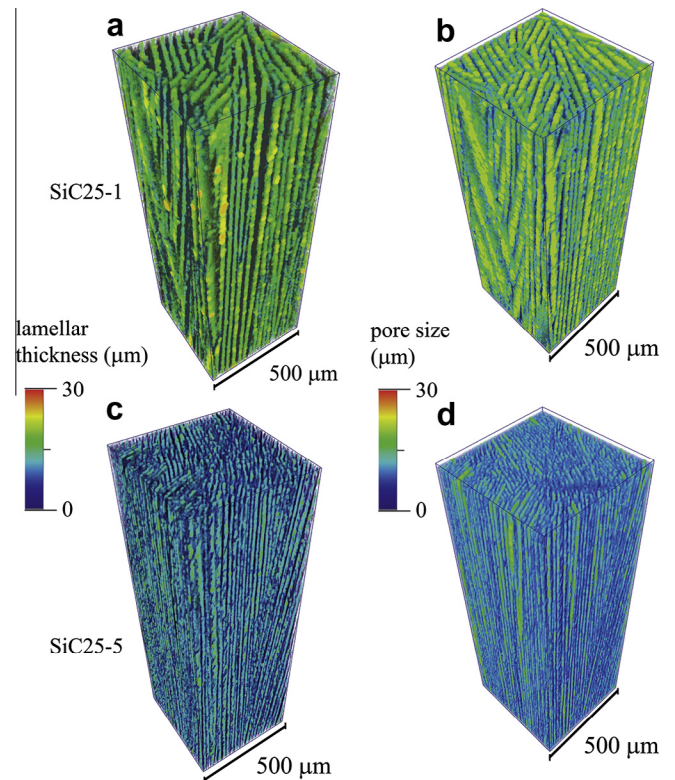


Fig. 6. Evaluation of structural parameters from the 3-D tomographic images of (a, b) SiC25-1 and (c, d) SiC25-5 scaffolds. The false colors represent (a, c) the lamella thickness and (b, d) the pore size. These parameters are constant along the samples, demonstrating the homogeneity of the scaffolds.

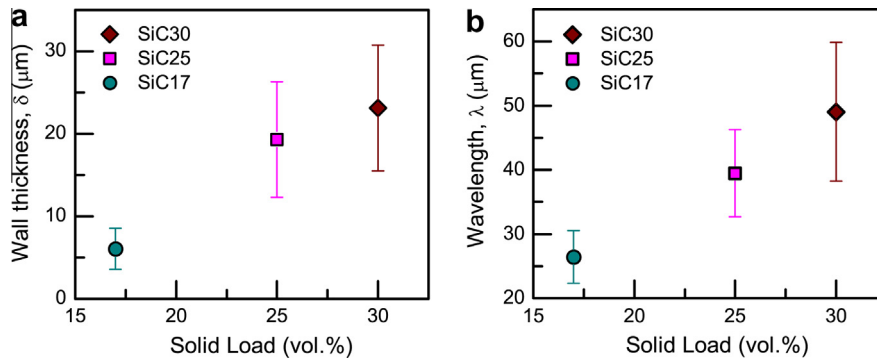


Fig. 7. (a) Lamella wall thickness and (b) wavelength vs. the solid load of the starting suspensions for SiC samples freeze-cast at a cooling rate of $-1\text{ }^{\circ}\text{C min}^{-1}$.

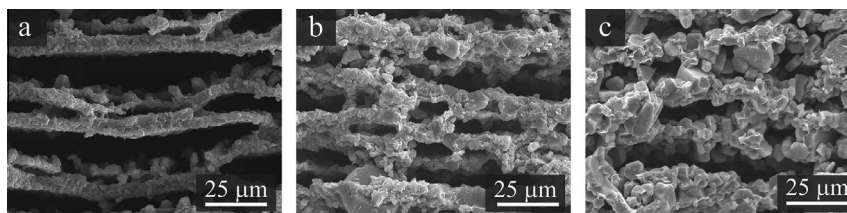


Fig. 8. SEM micrographs of (a) SiC17-5, (b) SiC25-5 and (c) SiC30-5 scaffolds, from suspensions with 17, 25 and 30 vol.% solid load, respectively, frozen at $-5\text{ }^{\circ}\text{C min}^{-1}$. The increase in suspension concentration induces a coarsening of the structure and a transition from (a) lamellar to (b, c) dendritic morphology. (c) The SiC30-5 scaffold exhibits the most intricate and disordered structure. The difference in the grain size for the samples is due to different sintering condition: SiC17-5 was sintered at $1850\text{ }^{\circ}\text{C}$ for 30 min, SiC25-5 at $1850\text{ }^{\circ}\text{C}$ for 1 h and SiC30-5 at $1900\text{ }^{\circ}\text{C}$ for 1 h. The different temperature did not affect the scaffold architectures, but only the grain size; indeed no residual porosity was observed in the ceramic wall for the three samples.

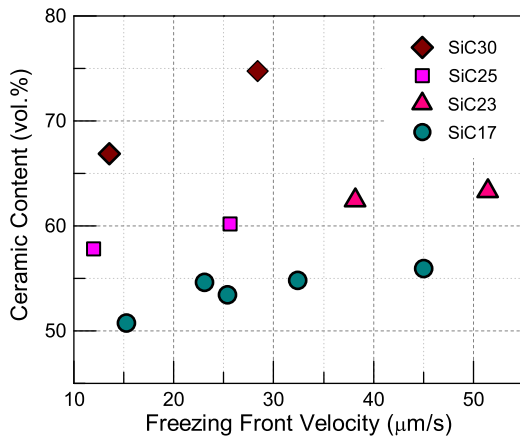


Fig. 9. Final ceramic content vs. freezing front velocity for SiC17, SiC23, SiC25 and SiC30 scaffolds obtained, respectively, from suspensions with 17, 23, 25 and 30 vol.% solid load. The ceramic content is clearly influenced by the suspension concentration and the cooling rate. Indeed for suspensions of same concentration, the samples frozen at faster cooling rate exhibit higher density.

result that the reduction in solidification velocity is minimized. By applying a linear cooling rate, the velocity of the freezing interface is higher at the beginning of the process, before stabilizing after a transition time to a constant value corresponding to a steady-state regime [45]. In this study, average freezing front velocities were calculated by dividing the freezing time by the height of each sample, although as the initial transition interval

was not considered, this may somewhat overestimate, by roughly 10% or so, the actual freezing velocities during the steady-state solidification.

4.2. Influence of freezing front velocity on lamella thickness and wavelength

The porosity pattern in a freeze-cast scaffold depends directly on the ice morphology developed during freezing. Consequently, the freezing parameters play a crucial role for the optimization of the structural properties of the scaffold. Measurements of the thickness δ and spacing λ of the lamellae (Fig. 3) support the general, and intuitive, trend that smaller ice crystals result from faster cooling rates and freezing front velocities.

As noted above, the pore morphology evolves from lamellar to dendritic with increasing cooling rate (Fig. 4). These observations are consistent with Harrison and Tiller's study [10] of the ice morphology and texture developed during the freezing of aqueous solutions, where the elongated cells of ice were reported to transform to a dendritic morphology as the degree of constitutional supercooling was increased. These authors argued that faster solid-liquid interface velocities led to steeper solute concentration gradients and larger constitutional supercooling; more rapid cooling thus promotes dendritic ice morphologies.

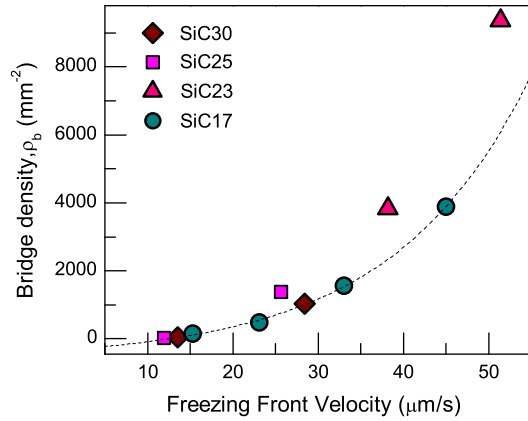


Fig. 10. Density of bridges between lamellae (number of bridges per unit area) vs. freezing front velocity for SiC17, SiC23, SiC25 and SiC30 scaffolds obtained, respectively, from suspensions at 17, 23, 25 and 30 vol.% solid load. The bridge density increases exponentially with the freezing front velocity.

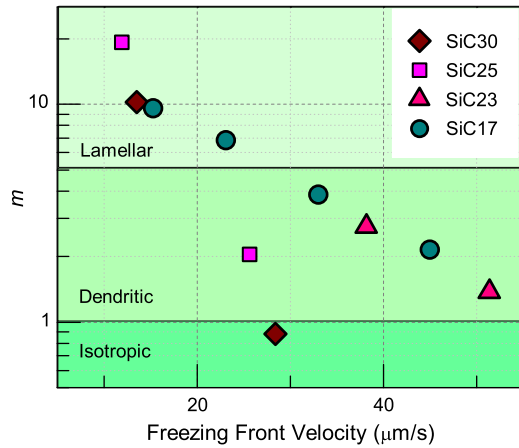


Fig. 11. Morphological parameter m vs. freezing front velocity for samples obtained from SiC17, SiC23, SiC25 and SiC30 suspensions, respectively, 17, 23, 25 and 30 vol.% solid load. The dimensionless parameter m , defined in Eq. (1) as $m = (1/\rho_b)/\lambda^2$, compares the bridge spacing and the lamella wavelength. In terms of the various freeze-cast morphologies, $m > 5$ for lamellar structures, $1 < m < 5$ for dendritic structures and $m < 1$ for isotropic structures.

4.3. Influence of solid load on lamella thickness and wavelength

Results for the lamella thickness δ and wavelength λ , plotted in Fig. 7 as a function of the solid load in the suspension, indicate that slurries with higher solid concentration lead to coarser scaffolds. We also observed that increases in solid load and cooling rate have a similar effect on the final morphology. The freezing velocity corresponding to the transition from lamellar to dendritic ice depends on the solid load in the suspension, and is inversely proportional to the slurry concentration. The transitions in the ice crystal morphology from planar to lamellar and from lamellar to isotropic are also sensitive to solid content, as reported by Waschkes et al. [41]. The dependence of the

ice crystal morphology on the suspension concentration can be related to the relationship between solid load, solidification temperature depression and constitutional supercooling. With increasing solid loads, the critical supercooling that triggers the transition in morphologies from planar to lamellar, or from lamellar to dendritic, is reached at a lower freezing velocity.

Similar conclusions can be made for the critical velocity, v_c , the velocity of the freezing front, above which the ceramic particles are entrapped into the ice; we observed that v_c decreases as the suspension concentration is raised. The critical velocity of the freezing front for particle entrapment can be expressed by the following expression [20,42]:

$$v_c = (\Delta\sigma d / 3\eta R) \times (a_o/d)^z \quad (2)$$

where $\Delta\sigma$ is the free energy of the particle, a_o is the average intermolecular distance in the liquid film between the particle and the solid front, d is the overall thickness of this film, η is the solution viscosity, R is the particle radius and z is an exponent that can vary from 1 to 5. As v_c is inversely proportional to the particle radius and the viscosity (which depends on the solid content [46]), the critical velocity would clearly be expected to be reduced with higher slurry concentrations.

4.4. Influence of solid load and freezing front velocity on ceramic content

From the results in Fig. 9, the ceramic content in the scaffolds can be seen to depend either on the suspension concentration or on the cooling rate. For samples from the same suspensions, the final ceramic content depends on the cooling rate.

Deville and Bernard-Granger [47] examined the effect of several parameters on the densification of ice-templated green bodies to clarify the role of the solvent. They compared the results reported in literature for freeze-cast samples obtained from aqueous or organic solvent-based suspensions, with emphasis on the influence of the surface tension, osmotic pressure, pores size and radius of curvature. Scaffolds obtained from camphene-based suspensions were less porous than the ones from aqueous slurries with equal solid content. Moreover the former samples exhibited highly dendritic and smaller pores, due to the different morphology of the camphene vs. water crystals. They concluded that the difference in the total porosity of aqueous and organic solvent-based systems was caused by two main factors: the variation of the solvent surface tension, which affects the particle packing, and the difference in the radius of curvature of the pores formed by the ice. Indeed, the final ceramic content is the result of the densification of the green scaffolds, which is controlled by the local radius of curvature of the pores. Mass transport phenomena associated with densification are promoted by a small radius of the curvature of the solid–vapor interface, i.e., by the curvature of the pores. In our samples, we observed a transition from lamellar to dendritic pore morphology, driven

by the cooling rate (Fig. 4). The dendritic pores (Fig. 4c and d), characterized by an intricate shape, have a smaller radius of curvature than the lamellar pores, which are larger and flat (Fig. 4a and b). Consequently, samples obtained at higher cooling rates, which exhibit dendritic rather than lamellar pores, experience a larger densification.

4.5. Morphology map

Based on this study, we can summarize our results on the form and morphology of silicon carbide scaffolds freeze-cast from aqueous suspensions in the form of a “morphology map”, which defines the relationships between the processing conditions and resulting structures. The diagram, presented in Fig. 12, can be divided into three regimes of processing conditions: those leading to lamellar structures, those to dendritic morphologies and finally the conditions for particle entrapment (forming isotropic morphologies). The suspension solid load and the cooling rate play a similar role in the development of the scaffold morphology; they affect the transition from planar to lamellar and from lamellar to dendritic morphologies. The interface velocity associated with these morphological transitions and the critical velocity, v_c , depend on the suspension concentration. The lamellar structure can be obtained with either low cooling rates or dilute suspensions. For intermediate combinations of the two parameters, a dendritic morphology is likely to be developed. High solid loads or fast cooling rates lead to particle entrapment in the ice, such that the unidirectional structure cannot be obtained.

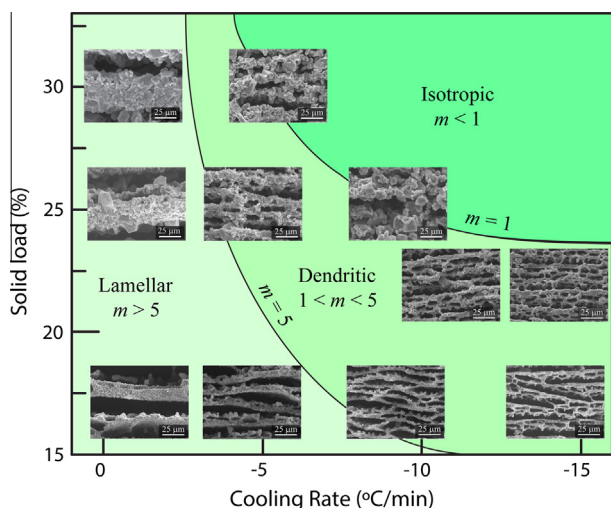


Fig. 12. Morphology map for freeze-cast SiC scaffolds. The diagram illustrates the structural evolution induced by varying the cooling rate and the suspension solid load. The microstructures, obtained under a broad range of processing conditions, differ in terms of lamella wavelength and density of bridges between the main lamellae. These differences are represented by the morphological parameter m , which compares the bridge spacing and the lamella wavelength. The three regimes of processing variables correspond to the conditions yielding lamellar ($m > 5$), dendritic ($1 < m < 5$) or isotropic ($m < 1$) structures.

From the perspective of mimicking natural materials such as nacre, such ceramic scaffolds have to be infiltrated with a small volume fraction of a compliant phase, such as a polymer, e.g., polymethyl methacrylate (PMMA) [27], or metal, e.g., Al–Si [48]. Although outside the scope of this paper, based on preliminary mechanical tests on the SiC scaffolds infiltrated with PMMA, the lamellar samples appeared the most suitable to mimic the mechanical behavior of nacre, providing the best compromise between strength (from the presence of the SiC lamellae) and toughness (from limited plastic deformation in the polymeric layers), which enabled limited pull-out and crack bridging. The dendritic samples, conversely, exhibited higher strength but lower toughness, the presence of many bridges between the lamellae hindered their sliding and limited the energy dissipation necessary for crack propagation resistance. A full mechanical characterization of the behavior of such polymer-infiltrated SiC scaffolds is currently in progress. However, we believe that the morphology map developed in this work for freeze-cast SiC scaffolds provides a crucial first step for the future development of these high-toughness biomimetic ceramics.

5. Conclusions

We have investigated the various morphologies of ceramic structures produced by the freeze casting of silicon carbide with the objective of generating scaffolds for the fabrication of nacre-like SiC composites. Such morphologies are of paramount importance for the creation of structural architectures with optimal mechanical performance, with lamellar scaffolds showing the most promise. The array of microstructures produced demonstrates the versatility and effectiveness of the ice-templating technique for the fabrication of SiC scaffolds with a wide range of lamella thicknesses, porosities and microstructures.

Based on this study, the following specific conclusions can be made:

1. The transition from a lamellar to a dendritic morphology in the freeze-cast SiC scaffolds, as well as the limit between particle rejection and entrapment, depends critically on the thermal conditions, the particle fraction in the suspension and the interface velocity, all factors which affect the degree of constitutional supercooling.
2. An increase in the cooling rate and/or the slurry concentration also triggers the transition from lamellar to dendritic morphology.
3. Since each processing parameter simultaneously affects many characteristics of the ceramic scaffolds, a morphology map was developed to define the regimes where the various morphologies of freeze-cast SiC-based scaffolds are formed as a function of these processing variables, specifically cooling rate and suspension solid content. Such maps provide essential guidance for the fabrication of biomimetic ceramic structures with various functional properties.

Acknowledgements

This work was supported by the Mechanical Behavior of Materials Program at the Lawrence Berkeley National Laboratory by the Office of Science, Office of Basic Energy Sciences, Division of Materials Sciences and Engineering, of the US Department of Energy under Contract No. DE-AC02-05CH11231. Thanks are due to Amy Wat for helpful discussions and to Dr. Robert Kostecky and Dr. Jaroslaw Syzdek for allowing us access to their high-temperature furnace.

References

- [1] Sofie SW, Dogan F. *J Am Ceram Soc* 2001;84(7):1459–64.
- [2] Araki K, Halloran JW. *J Am Ceram Soc* 2001;87(10):1859–63.
- [3] Araki K, Halloran JW. *J Am Ceram Soc* 2004;87(11):2014–9.
- [4] Fukasawa T, Deng ZY, Ando M, Ohji T, Goto Y. *J Mater Sci* 2001;36:2523–7.
- [5] Yokoyama F, Achife EC, Momoda J, Shimamura K, Monobe K. *Colloid Polym Sci* 1900;268:552–8.
- [6] Schoolf H, Bruns L, Fischer A, Heschel I, Rau G. *J Cryst Growth* 2000;209:122–9.
- [7] Fukasawa T, Ando M, Ohji T, Kanzaki A. *J Am Ceram Soc* 2001;84(1):230–2.
- [8] Deville S, Saiz E, Nalla RK, Tomsia AP. *Science* 2006;311:515–8.
- [9] Mukai SR, Nishihara H, Tamon H. *Microporous Mesoporous Mater* 2008;116:166–70.
- [10] Harrison JD, Tiller WA. *J Appl Phys* 1963;34(11):3349–55.
- [11] Terwillinger JP, Dizio SF. *Chem Eng Sci* 1970;25:1331–49.
- [12] Tanner JE. *Cryobiology* 1975;12:353–63.
- [13] Worster MG, Wettlaufer JS. *J Phys Chem B* 1997;101:6132–6.
- [14] Korber C, Rau G, Cosma MD, Cravalho EG. *J Cryst Growth* 1985;72:649–62.
- [15] Casses P, Axouli-Aidi MA. *Adv Colloid Interface Sci* 1994;50:103–20.
- [16] Zhang H, Hussain I, Brust M, Butler MF, Pannard SP, Cooper AL. *Nat Mater* 2005;4:787–93.
- [17] Munch E, Saiz E, Tomsia AP, Deville S. *J Am Ceram Soc* 2009;92(7):1534–9.
- [18] Deville S. *Adv Eng Mater* 2008;10(3):155–69.
- [19] Pekor CM, Kisa P, Nettleship I. *J Am Ceram Soc* 2008;91(10):3185–90.
- [20] Deville S, Saiz E, Tomsia AP. *Acta Mater* 2007;55:1965–74.
- [21] Deville S, Maire E, Lasalle A, Bogner A, Gauthier C, Leloup J, et al. *J Am Ceram Soc* 2010;93(9):2507–10.
- [22] Preiss A, Su B, Collins S, Simpson D. *J Eur Ceram Soc* 2012;32:1575–83.
- [23] Lasalle A, Guizard C, Leloup J, Deville S, Marie E, Bogner A, et al. *J Am Ceram Soc* 2012;95(2):799–804.
- [24] Li WL, Lu K, Walz JY. *Intl Mater Rev* 2012;57(1):37–60.
- [25] Wegst UGK, Ashby MF. *Philos Mag* 2004;84(21):2167–81.
- [26] Wang C, Huang Y, Zan Q, Guo H, Cai S. *Mater Sci Eng C* 2009;11:9–11.
- [27] Munch E, Launey ME, Alsem DH, Saiz E, Tomsia AP, Ritchie RO. *Science* 2008;5:1516–20.
- [28] Tang J, Chen Y, Wang H, Liu H, Fan Q. *Key Eng Mater* 2005;280–283:1287–90.
- [29] Yoon B, Lee E, Kim H, Koh Y. *J Am Ceram Soc* 2007;90(6):1753–9.
- [30] Greskovich G, Rosolowski JH. *J Am Ceram Soc* 1976;59(7–):336–43.
- [31] Lange FF. *J Mater Sci* 1975;10:314–20.
- [32] Omori M, Takei H. *J Mater Sci* 1988;23:3744–9.
- [33] Mulla MA, Krstic VD. *J Mater Sci* 1994;29:934–8.
- [34] She JH, Ueno K. *Mater Res Bull* 1999;34:1629–36.
- [35] Castillo-Rodriguez M, Munoz A, Dominguez-Rodriguez A. *J Eur Ceram Soc* 2006;26:2397–405.
- [36] Zhang T, Zhang Z, Zhang J, Jiang D, Lin Q. *Mater Sci Eng A* 2007;443:257–61.
- [37] Nader M, Aldinger F, Hoffmann MJ. *J Mater Sci* 1999;34:1197–204.
- [38] Eom JH, Kim YW, Song IH. *J Eur Ceram Soc* 2012;32:1283–90.
- [39] Gilbert CJ, Cao J, MoberlyChan WJ, DeJonghe LC, Ritchie RO. *Acta Mater* 1996;44:3199–214.
- [40] Rao RR, Roopa HN, Kannan TS. *Ceram Intl* 1999;25:223–30.
- [41] Waschkie T, Oberacker R, Hoffmann MJ. *Acta Mater* 2011;59:5125–45.
- [42] Wegst UGK, Schecter M, Donius AE, Hunger PM. *Phil Trans Roy Soc A* 2010;368:2099–121.
- [43] Waschkie T, Oberacker R, Hoffmann MJ. *J Am Ceram Soc* 2009;92(S1):S79–84.
- [44] Bareggi A, Maire E, Lasalle A, Deville S. *J Am Ceram Soc* 2011;94(10):3570–8.
- [45] Deville S, Maire E, Lasalle A, Bogner A, Gauthier C, Leloup J, et al. *J Am Ceram Soc* 2009;92(11):2489–96.
- [46] Muller S, Llewellyn EW, Mader HM. *Proc Roy Soc A* 2010;466:1201–28.
- [47] Deville S, Bernard-Granger G. *J Eur Ceram Soc* 2011;31:983–7.
- [48] Launey ME, Munch E, Alsem DH, Saiz E, Tomsia AP, Ritchie RO. *J Roy Soc Interface* 2010;7:741–53.